Weld Crack Detection Based on Region Electromagnetic Sensing Thermography

Yingchun Wu, Bin Gao, *Senior Member, IEEE*, Jian Zhao, Yizhe Wang, Zewei Liu, Juan Chen, Ying Yin, and Gui Yun Tian, *Senior Member, IEEE*

***Abstract*— Nondestructive inspection for fatigue cracks is a critical and challenge task in both science and industry fields. This paper investigates the sensing effect of region electromagnetic performance as well as thermal intensity and uniformity on weld crack detection. The uniformity variation caused by vertical and horizontal lift-off distance between sensing and defect has been studied. In particular, a new ΔT metric has been proposed to present the thermal contrast and evaluate the detectability for weld natural cracks. This has been conducted by detail interpreting the region sensing for electromagnetic and thermal fields. Results have shown that the crack can be detected with a higher thermal contrast as it lies in a region sensing with relatively high uniformity and eddy current intensity.**

***Index Terms*— Region electromagnetic sensing thermography, weld fatigue crack, nondestructive inspection, uniformity variation.**

I. Introduction

With the rapidly development of industry, the threat from the natural cracks produced during manufacture and in-service of materials has received considerable attention. Nondestructive testing (NDT) plays an essential role in guaranteeing the safety and reliability of the structure [1].

Magnetic Particle Testing (MT), Penetration Testing (PT) and Ray Testing (RT) are the main NDT methods in crack detection. MT is effective for the surface and near-surface crack detection. However, the detection procedure of MT is complicated and it only works for ferromagnetic material [2]–[4]. PT is sensitive to opening surface crack [5]–[7]. However, the penetrant process requires to be cleaned and it produces pollution to the environment. RT can obtain intuitive results whereas the radiation is a potential issue [8]–[10]. Recently, the electromagnetic thermography has attracted increasingly attention as it enables to conduct a rapid inspection over a large area with high spatial resolution and sensitivity. In addition, the detection work can be finished in a short period of time and there are none consumables and pollution. As an emerging integrative NDE technique, Eddy Current Pulsed Thermography (ECPT) [11]–[14] combines the advantages of both eddy current [15] and infrared thermography [16]. It is widely used in the detection of damages including corrosion in steel, rolling contact fatigue (RCF) cracks in rail and welding cracks in pressure vessels, boilers and pipelines [17]–[20].

Fatigue cracks often originate in enduring intense stress concentration on welds and appear under long-term continuous alternating loading [21]. Due to the rough surface and the complicated shape of the weld, it is difficult to detect the cracks from the complex mixing signals. The influence factors include a strong background noise, non-uniform thermal emission and non-zero conductivity.

It can be seen that the problems of in-homogenous heating and the blocking effect due to the placement of the ECPT coil remain as challenges for accurately detecting the natural defects [22]–[24]. Thus, significant works have been conducted in the optimization of inductor shape and excitation parameters [25]. Lahiri *et al.* reported low frequency alternating magnetic field for thermographic NDE [26]. Shen *et al.* studied the effects of the heating parameters, such as the lift-off distance, the exciting current, the frequency and the turns of the coil on the temperature histories [27]. Gao *et al.* conducted the gear rolling fatigue evaluation by using the line coil [22]. Oswald-Tranta detected surface crack of metallic material by using the helix coil [28]. Li and Peng *et al.* proposed Helmholtz-coil based ECPT configuration to electrical component and rail damages detection [23], [29]. Tsopelas *et al.* used planar circular coil for crack detection on aluminum plate [30]. Gao *et al.* proposed a ferrite-yoke based ECPT to obtain an open field imaging for defect quantitative evaluation [31], [32]. Hansen *et al.* designed an asymmetric induction coil for generating a uniform heating [33].

Modifying the inductor shape or optimizing the exciting parameters can enhance the detectability for cracks with different directions. However, uniform heating essentially requires the relatively uniform distribution for both magnetic and eddy current fields. Thus, this paper investigates the region sensing effect for the distribution of the electric, magnetic and thermal

Manuscript received July 30, 2018; accepted August 21, 2018. Date of publication September 10, 2018; date of current version December 21, 2018. This work was supported in part by the Science and Technology Department of Sichuan, China, under Grant 2018JY0655, in part by the National Natural Science Foundation of China under Grant 61401071 and Grant 61527803, in part by NSAF under Grant U1430115, and in part by the EPSRC IAA Phase 2 Funded Project: "3D Super-Fast and Portable Eddy Current Pulsed Thermography for Railway Inspection" under Grant EP/K503885/1. The associate editor coordinating the review of this paper and approving it for publication was Prof. Boby George. *(Corresponding author: Bin Gao.)*

Y. Wu, B. Gao, J. Zhao, Y. Wang, and Z. Liu are with the School of Automation Engineering, University of Electronic Science and Technology of China, Chengdu 611731, China (e-mail: bin_gao@uestc.edu.cn).

J. Chen and Y. Yin are with the Sichuan Special Equipment Inspection Institute, Chengdu 610061, China.

G. Y. Tian is with the School of Electrical and Electronic Engineering, Newcastle University, Newcastle upon Tyne NE1 7RU, U.K.

Digital Object Identifier 10.1109/JSEN.2018.2868867

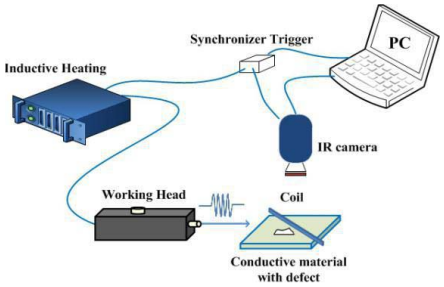

Fig. 1. The schematic diagram of ECPT system.

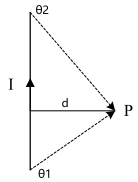

Fig. 2. Magnetic field at a point P due to a finite length current carrying conductor.

fields. Different lift-off distance and region effect between sensing-defect are considered. These studies enable us to build the physic context connected between the local and the global electromagnetic thermal region sensing model which benefits the detection on weld cracks. It provides a possibility to dramatically increasing the thermal contrast between the defect and non-defect areas for weak thermal signal detection.

The rest of this paper has been organized as follows. Section 2 describes the basic theory of ECPT, the boundary conditions of the magnetic field and the derivation of a new ΔT metric for region sensing in the electromagnetic and thermal field. Section 3 implements the simulation and experiment studies. Section 4 concludes the study and outlines the future work.

II. Methodology

A. Introduction of ECPT System

The schematic diagram of the ECPT system is shown in Fig.1. High frequency alternating current generated by the excitation module is driven to the coil. It induces the eddy current and generates the resistive heat in the conductive material. The three-dimensional heat diffusion leads to the flow from high to low temperature area. This reduces the contrast until the heat reaches equilibrium in the material. If a discontinuity exists in the conductive material, the distribution of eddy current and the process of thermal diffusion will be disturbed. Subsequently, the variation of the surface heat distribution can be captured by an infrared camera [34].

B. Discussion of Region Electromagnetic Field

As shown in Fig.2, according to Biot-Savart law, the magnetic field at point P can be calculated as

$$B = \frac{\mu_0 I}{4\pi d}(\cos\theta_1 - \cos\theta_2) \tag{1}$$

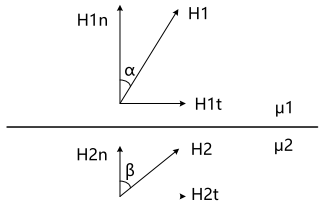

Fig. 3. Graphical representation of the relations between components of H at an interface.

where μ_0 denotes the magnetic permeability of vacuum and it equals to $4\pi \times 10^{-7}\mathrm{N}\cdot\mathrm{A}^{-2}$, I denotes the current intensity, d denotes the distance between the point and the conductor, θ_1, θ_2 denote the angles between the dotted line connecting the two ends of the conductor to the point P and the conductor, respectively.

Fig.3 shows the relationship between the magnetic field vectors at the interface of a medium and a material. H_{1t}, H_{2t} are the tangential components of H_1 and H_2, H_{1n}, H_{2n} are the normal components of H_1 and H_2. μ_1, μ_2 are the magnetic permeability of the two media. α, β are the angles between H and the normal component on each side of the interface, respectively. At the media boundary, the field vectors are discontinuous and their behaviors across the boundary are governed by the boundary conditions:

$$\mu_1 H_{1n} = \mu_2 H_{2n} \quad H_{1t} = H_{2t} \tag{2}$$

It can be seen from Fig.3 that

$$\tan\alpha = \frac{H_{1t}}{H_{1n}} \quad \tan\beta = \frac{H_{2t}}{H_{2n}} \tag{3}$$

Considering the constitutive equations, namely

$$\frac{\tan\alpha}{\tan\beta} = \frac{\mu_1}{\mu_2} \tag{4}$$

When a surface current flows at the interface from the two magnetic materials, the tangential components of the magnetic field will be discontinuous. Instead, they are related by the boundary condition:

$$\hat{a}_n \times (H_{1t} - H_{2t}) = J_s \tag{5}$$

where $\hat{a}_n$ is the normal unit vector. Eqn.5 shows that H_{1t} and H_{2t} are orthogonal to J_s, and the difference between $|H_{1t}|$ and $|H_{2t}|$ is $|J_s|$.

Since a source region in a media, the wave equation of E and H are

$$\nabla^2 E - \mu\varepsilon\frac{\partial^2 E}{\partial t^2} = \mu\frac{\partial J}{\partial t} + \frac{\nabla\rho}{\varepsilon} \tag{6}$$

$$\nabla^2 H - \mu\varepsilon\frac{\partial^2 H}{\partial t^2} = -\nabla \times J \tag{7}$$

where ρ is the free charge density at the surface of the material. Here ρ equals to 0. E and H can be solved by introducing a potential function.

As can be seen in Fig.4, Vrana *et al.* [35] investigates the distribution of eddy current on the surface of the conductive material by considering a simple model who consists of an inductor and a sample. A straight wire inductor is applied.

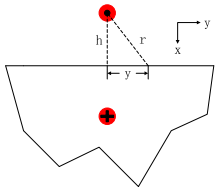

Fig. 4. Model for calculating the distribution of eddy current on the conductive body.

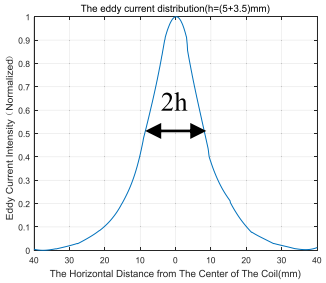

Fig. 5. The distribution of eddy current density on the surface.

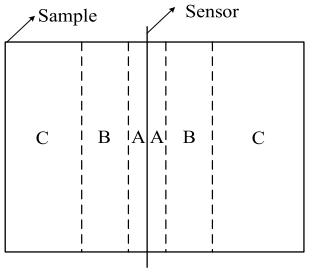

Fig. 6. The three regions with different distribution characteristic of the eddy current (Top view).

The sample is large enough to be approximated as a semi-finite body. Results have illustrated that the distribution of the eddy current in a line orthogonal to the coil on the surface follows a Lorentzian shape as shown in Fig.5. The full width half maximum of this distribution is two times the distance between the center of the coil and the surface of the sample, which is denoted by h. Notably, h is the sum of the radius of the coil and the lift-off distance between the coil and the sample.

Fig.6 shows the distribution of the eddy current with seven different values of h. Considering a small region near the sensor on the surface of the sample, it can be seen from Fig.5 and Fig.6 that with the vertical lift-off distance or the horizontal distance between sensing and the center of the region increasing, the eddy current intensity drops while the uniformity enhances. Fig.7 shows the top view of the sample, the sensor is denoted by a line in the center of the sample. There are three regions on the surface with different distribution characteristic of the eddy current. Region A has high eddy current intensity whereas with low uniformity, region B has relatively high uniformity eddy current and the intensity of the eddy current is sufficient. Finally, the eddy current in region C is too weak for detection.

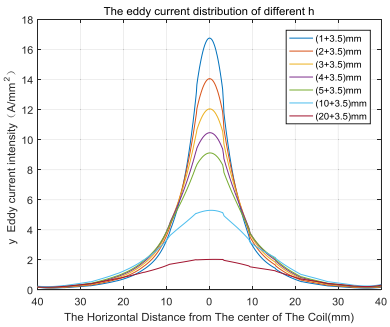

Fig. 7. The distribution of eddy current under different h.

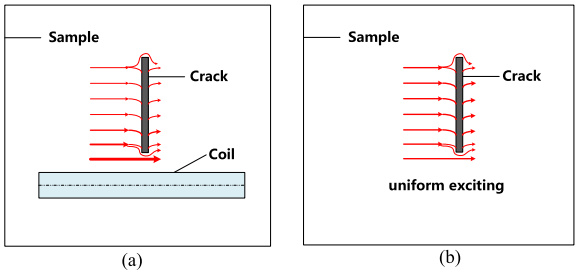

Fig. 8. Eddy current path (Top view). (a) Line coil exciting. (b) An ideal uniform exciting.

The uniformity of the eddy current is measured by regional variance:

$$S = \frac{1}{Nx}\frac{1}{Ny}\sum_{i=1}^{Nx}\sum_{j=1}^{Ny}(J_{i,j} - \mu)^2 \tag{8}$$

where Nx and Ny denote the number of the sampling points in the parallel direction and the vertical direction, respectively. $J_{i,j}$ denotes the eddy current intensity of the point (i, j), μ denotes the average eddy current in the region.

When a defect exists on the surface of the sample, the eddy current will be disturbed by the crack since the conductivity and permeability varied. Fig.8 shows the distribution of the eddy current around the crack. The width of the red line is proportional to the value of the eddy current. Fig.8 (a) shows the non-uniformity caused by different horizontal distance from the exciting coil. In particular, the upper side of the crack is far from the exciting coil. This will lead to the lower intensity of the eddy current. On the other hand, the lower side of the crack which near the exciting coil will lead to the higher intensity. Fig.8 (b) shows the eddy current path around the crack which lies in an ideal area under the relative uniform eddy current field.

Comparing Fig.8 (a) and (b), the variation of the eddy current intensity affect the detection performance as the disturbance around the crack excited by a line coil is more difficult to be caught than the ideal uniform exciting. Thus it is critical to sensing a relatively uniform region in order to eliminate the detection error caused by the non-uniformity of the eddy current boundaries.

The above analysis explicitly illustrated that there are region interaction between the coil placement and defects. As general

detection methods are mostly established where the location of cracks is assumed known as a priori, it causes practical issue to use induction thermography without discussing the eddy current intensity. Thus, it becomes necessary to provide a specific discussion of the detection effect between the region eddy current and cracks.

C. Thermal Field

Due to Joule heating, the temperature of the conductive material increases. The sum of the generated heat Q is proportional to the square of the eddy current density J_s. The current density, in turn, is proportional to the electric field intensity vector E. This relationship can be expressed by

$$Q = \frac{1}{\sigma}|J_s|^2 = \frac{1}{\sigma}|\sigma E|^2 \tag{9}$$

By taking account of Joule heating and heat diffusion, the heat conduction equation of a specimen can be expressed as

$$\frac{\partial T}{\partial t} = \frac{\lambda}{\rho C_p}\left(\frac{\partial^2 T}{\partial x^2} + \frac{\partial^2 T}{\partial y^2} + \frac{\partial^2 T}{\partial z^2}\right) + \frac{1}{\rho C_p} q(x, y, z, t) \tag{10}$$

where $T = T(x, y, z, t)$ is the temperature distribution, λ is the thermal conductivity of the material. ρ is the density, C_p is the specific heat capacity. $q(x, y, z, t)$ is the internal heat generation function per unit volume and unit time, which is the result of the Joule heating by eddy current [13].

D. Derivation of a New Metric

To discuss the thermal contrast between the defect region and the contiguous non-defect region, a new ΔT metric is proposed. Comparing with conventional Area-Weighted Average temperature difference ($AWA\Delta T$), the new ΔT metric includes various effects due to the target and background characteristics in a temperature scene image. These consist of evaluating the number of pixels, the mean and variance on the target and background temperatures [36], [37].

The new ΔT metric is defined as:

$$\Delta T = \sigma_{T|S} - \sigma_{B|S} \tag{11}$$

where $\sigma_{T|S}$ and $\sigma_{B|S}$ denote the standard deviation of target pixel temperature conditioned on the mean temperature of scene and the standard deviation of background pixel temperatures conditioned on the mean temperature of scene, respectively.

To formulate the new ΔT metric equation, the mean and variance of the pixel temperatures on target, background and scene are expressed, namely

$$\mu_T = \frac{1}{N_T}\sum_{i=1}^{N_T} P_i^T \quad \sigma_T^2 = \frac{1}{N_T}\sum_{i=1}^{N_T}(P_i^T - \mu_T)^2 \tag{12}$$

$$\mu_B = \frac{1}{N_B}\sum_{i=1}^{N_B} P_i^B \quad \sigma_B^2 = \frac{1}{N_B}\sum_{i=1}^{N_B}(P_i^B - \mu_B)^2 \tag{13}$$

$$\mu_S = \frac{1}{N_S}\sum_{i=1}^{N_S} P_i^S \quad \sigma_S^2 = \frac{1}{N_S}\sum_{i=1}^{N_S}(P_i^S - \mu_S)^2 \tag{14}$$

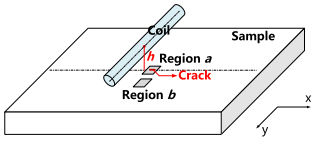

Fig. 9. The three-dimension model of defective sample detecting.

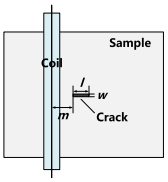

Fig. 10. The top view of the model.

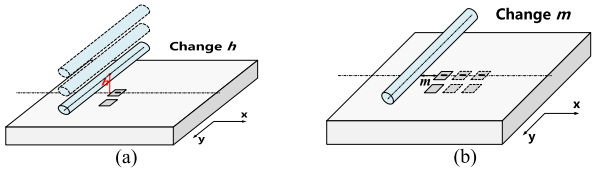

Fig. 11. The calculating model. (a) Various vertical lift-off distance. (b) Various horizontal distance.

where P_i^T, P_i^B, P_i^S denote the pixel temperature on target, background and scene, N_T, N_B, N_S denote the number of pixels on target, background and scene. It is noted that $N_S = N_T + N_B$. Then $\sigma_{T|S}^2$ and $\sigma_{B|S}^2$ can be expressed as

$$\sigma_{T|S}^2 = \frac{1}{N_T}\sum_{i=1}^{N_T}(P_i^T - \mu_S)^2 = \sigma_T^2 + \mu_T^2 - 2\mu_T\mu_S + \mu_S^2 \tag{15}$$

$$\sigma_{B|S}^2 = \frac{1}{N_B}\sum_{i=1}^{N_B}(P_i^B - \mu_S)^2 = \sigma_B^2 + \mu_B^2 - 2\mu_B\mu_S + \mu_S^2 \tag{16}$$

Thus the new ΔT metric in Eqn.11 can be rewritten as

$$\Delta T = \frac{1}{N_S}\left[\sqrt{N_s^2\sigma_T^2 + N_B^2 \times (\mu_T - \mu_B)^2} - \sqrt{N_s^2\sigma_B^2 + N_T^2 \times (\mu_B - \mu_T)^2}\right] \tag{17}$$

III. Experiment Set-Up

A. Numerical Simulation

In order to insight the uniformity variation caused by vertical and horizontal lift-off distance, several simulations including the surface and internal crack detection are implemented by inductive heating module in COMSOL Multiphysics. In the simulations, the wire diameter of the drive coil is 3.5mm, the height of the coil is 200mm. The excitation frequency is 256kHz, and the exciting current is 300A. The electromagnetic parameters of the test specimen are shown in Table I. The conductivity and the permeability are not fixed. The conductivity is initial conductivity and shift as [38, eq. (2)]. The permeability depends on the temperature

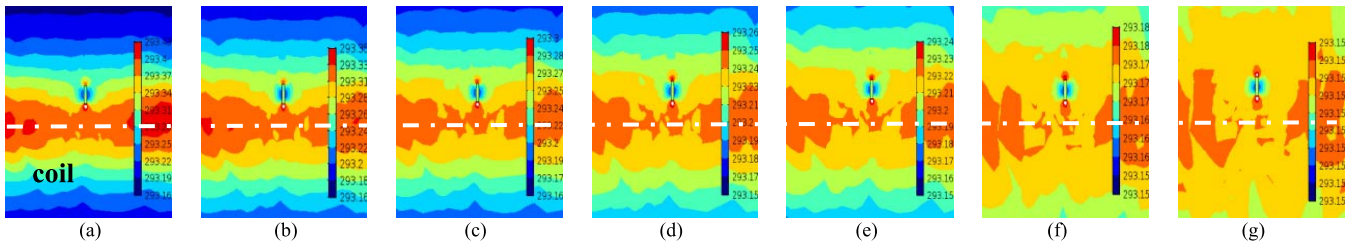

Fig. 12. Isothermal chart of various vertical lift-off distance (surface crack). (a) h = 1 + 3.5mm. (b) h = 2 + 3.5mm. (c) h = 3 + 3.5mm. (d) h = 4 + 3.5mm. (e) h = 5 + 3.5mm. (f) h = 10 + 3.5mm. (g) h = 20 + 3.5mm.

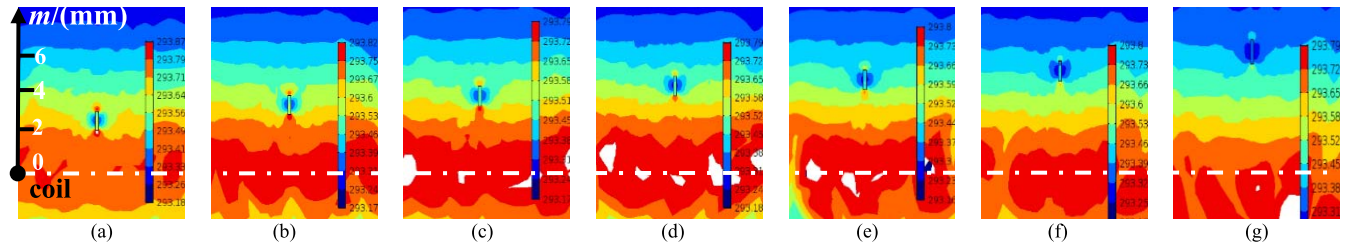

Fig. 13. Isothermal chart of various horizontal distance between sensing and defect (surface crack). (a) m = 2mm. (b) m = 3mm. (c) m = 3.5mm. (d) m = 4mm. (e) m = 4.5mm. (f) m = 5mm. (g) m = 6mm.

TABLE I
ELECTROMAGNETIC PARAMETERS OF MATERIAL

Parameters	value
Conductivity (S/m)	1.370e7
Relative permeability	1
Density (kg/m3)	8030
Heat capacity (J/(kg K))	502
Thermal conductivity (W/(m K))	12.1

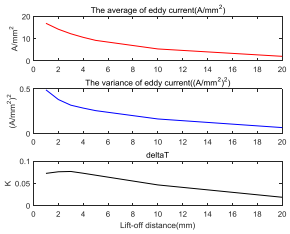

Fig. 14. The eddy current characteristic of non-defective sample and of defective sample under different vertical lift-off distance (surface crack).

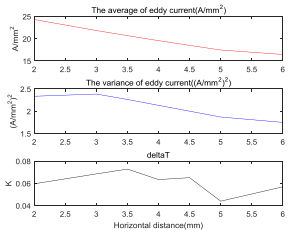

Fig. 15. The eddy current characteristic of non-defective sample and of defective sample under different horizontal distance (surface crack).

and the altering magnetic field. The influence of the temperature can be neglected as the heating is far less than Curie temperature [39], [40].

The overall interpretation from the various aspects in the detection procedure by discussing the effect between the region eddy current and defects is provided by Fig.9, 10 and 11, respectively.

Specifically, Fig.9 shows the fundamental three-dimensional model of scanning for the defective sample. Region a is the defective area of $2 \times 1mm^2$, region b is a non-defective area near region a. h denotes the vertical distance between the center of the coil and the surface of the sample. When calculating the thermal contrast by Eqn.17, region a is the target area and region b is the background area.

Fig.10 is the top view of the three-dimensional model of the Fig.9. This figure shows the relative position between the coil and the specimen. m denotes the horizontal distance between the center of the coil and the tip of the crack. w and l denote the width and length of the crack, respectively. Since the size of natural cracks are small (several hundred μm), the size of the crack is set as $l \times w \times d = 1\text{mm} \times 0.2\text{mm} \times 0.3\text{mm}$.

Fig.11 shows the calculating model. Change the value h and m, the effect of different vertical and horizontal lift-off distance can be obtained.

To deeply analyze the eddy current distribution, the average and the variance of the eddy current value in region a of the non-defective sample are separately calculated to represent the intensity and the uniformity of the eddy current distribution.

1) Simulations of Surface Crack: The isothermal charts with different vertical and horizontal lift-off distance between sensing and defect are shown in Fig.12 and Fig.13, respectively.

The orange region in Fig.12 is beneath the line coil. It can be seen that with the vertical lift-off distance increasing, the maximum temperature drops from 293.43 °C to 293.15 °C. On the other hand, the hot pot of the crack near the coil is submerged by the orange region initially, then it is separated from the lower temperature gradually and seems like a hot

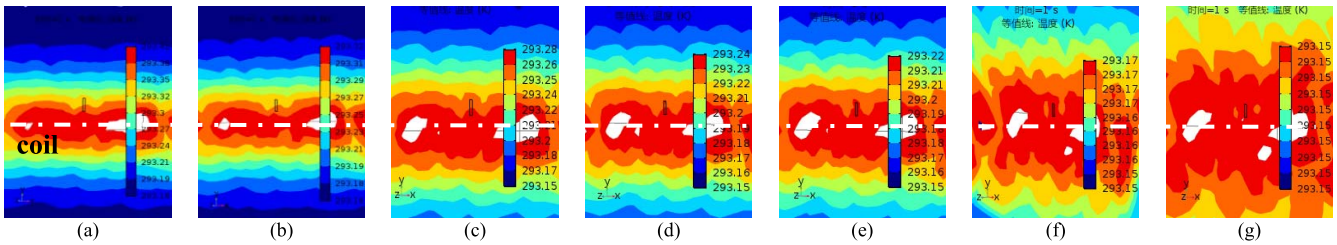

Fig. 16. Isothermal chart of various vertical lift-off distance (internal crack). (a) h=1+3.5mm. (b) h = 2 + 3.5mm. (c) h = 3 + 3.5mm. (d) h = 4 + 3.5mm. (e) h = 5 + 3.5mm. (f) h = 10 + 3.5mm. (g) h = 20 + 3.5mm.

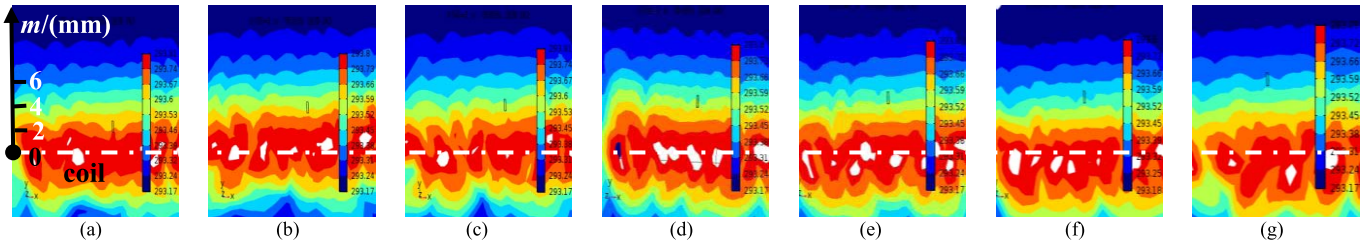

Fig. 17. Isothermal chart of various horizontal distance between sensing and defect (internal crack). (a) m = 2mm. (b) m = 3mm. (c) m = 3.5mm. (d) m = 4mm. (e) m = 4.5mm. (f) m = 5mm. (g) m = 6mm.

pot (h = 10mm). To compare the thermal contrast with different lift-off distance, the proposed ΔT metric (Eqn.17) is calculated.

Fig.14 shows the eddy current intensity and uniformity of non-defective sample and ΔT of defective sample under the different vertical lift-off distance. It can be seen from Fig.14 that with the vertical lift-off distance increasing, the eddy current intensity decreases and the uniformity of the eddy current distribution is enhanced. The ΔT between the region a and b in defective sample increased first and then decreased. The maximum ΔT is 0.766 at the lift-off distance of 3mm. When the lift-off distance increases from 1mm to 3mm, the uniformity is the main factor that affects the thermal contrast. Once the lift-off distance beyond 3mm, the eddy current intensity is too small to detect the object crack efficiently, thus it becomes the main factor.

In order to generate an ideal condition to discuss the detection effect of the region eddy current, Fig.13 is carried out under a fixed lift-off distance at 5mm, the exciting current is 900A. The reason is drawn as both density and uniformity of the eddy current affect the detecting result [41]. With the lift-off distance increasing, the concentricity of the eddy current distribution reduces while the bandwidth increases. If the distance is set too small, the eddy current reduces sharply in which it is far beyond the effect caused by uniformity. Thus, a bigger bandwidth setting is necessary to balance the intensity and uniformity. Meanwhile, a higher current is required to enhance the eddy current. It can be seen from Fig.13 that when m increases from 2mm to 3.5mm, the hot pot of the crack is submerged by the orange region, and the region seems to be expanded to the tip of the crack. When the distance becomes to 4mm, the hot pot can be seen clearly with rare noise. With further increasing of the distance, the hot pot is again unclear as the intensity of the eddy current is small.

Fig.15 illustrates the calculated intensity and variance of the eddy current in non-defective sample and ΔT in defective sample, respectively. Results have shown that with the distance increasing, the intensity of eddy current decreases, the variance of the eddy current drops (excepted for 2mm), and the ΔT is not monotonic. This is due to the interaction of the intensity and the non-uniformity of the eddy current.

The above analysis of the simulations have revealed that when increasing the vertical or the horizontal lift-off distance between sensing and defect, the eddy current intensity decreased and the uniformity of the eddy current enhanced. During the process, both intensity and non-uniformity act on the detection. Thus it is critical to obtain a region with relatively high uniformity and intensity of eddy current in crack detecting. In these simulations, the optimal distance in the two circumstance is summarized as follow:

1) When the region a (Fig.9) near the exciting coil is fixed, the optimal vertical lift-off distance is 3mm;
2) When the vertical lift-off distance is fixed at 5mm, the optimal horizontal distance between sensing and defect is 4mm.

2) Simulations of the Internal Crack: In order to investigate the effectiveness of the proposed region electromagnetic sensing thermography for internal crack, simulations of the subsurface crack are implemented. The hide depth of the crack is 0.01mm. The isothermal charts for various vertical and horizontal lift-off distance are shown in Fig.16 and Fig.17, respectively. The intensity and uniformity of the eddy current in non-defective sample have been compared and the thermal contrast of the internal crack has been calculated. These are shown in Fig.18 and Fig.19, respectively.

From the result, it can be seen that with the vertical lift-off distance increasing, the eddy current intensity decreased, the uniformity of the eddy current distribution enhanced and tends

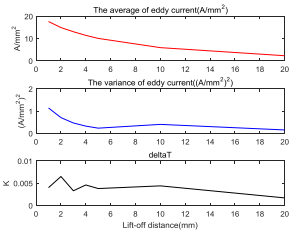

Fig. 18. The eddy current characteristic of non-defective sample and of defective sample under different vertical lift-off distance (internal crack).

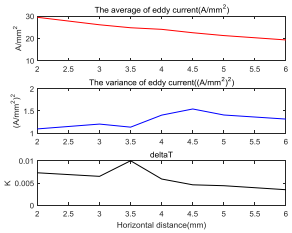

Fig. 19. The eddy current characteristic of non-defective sample and of defective sample under different horizontal distance (internal crack).

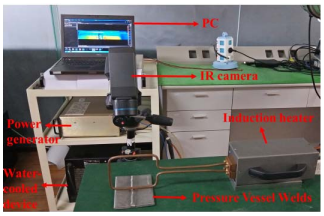

Fig. 20. Experiment set-up.

to be stable. When the lift-off distance increases from 1mm to 10mm, the uniformity affects the thermal contrast obviously. Once the lift-off distance beyond 10mm, the thermal contrast reduces, the uniformity has rarely impact on crack detection. When the horizontal distance increasing, the eddy current density decreases and the uniformity is not monotonous. The thermal contrast is the highest at 3.5mm.

B. Experiment Validation

In order to verify the above simulation studies, validation experiments are implemented. The system structure is shown in Fig.20. It includes the Easyheat 224 induction heater, the FLIR infrared camera, the water-cooled device, and the host computer. The temperature sensitivity is 0.08k. The frame rate of the IR camera is 200Hz. The excitation current is 480A, which is corresponding to the maximum exciting current in the experiment system. The exciting time is 300ms. Adjusting the exciting time will affect the generated temperature profile and the heating efficiency in the test sample. In addition, increasing the excitation period has a little effect on the detection [41]. As the optimal observation time is at the beginning of the excitation, this is chosen as 300ms.

The test sample is a weld of pressure vessel. The schematic model is shown in Fig.21, the weld reinforce is 2mm, h denotes the distance between the coil and the surface of

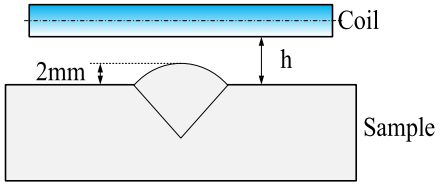

Fig. 21. The schematic model of the sample.

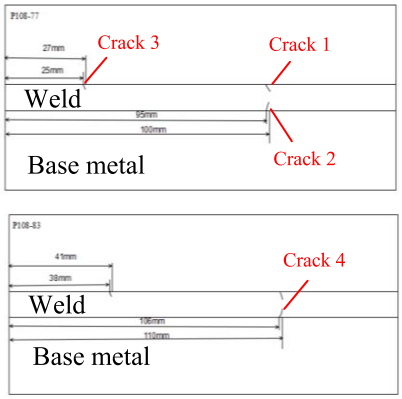

Fig. 22. The model of the weld cracks. (a) The original picture. (b) The amplified result.

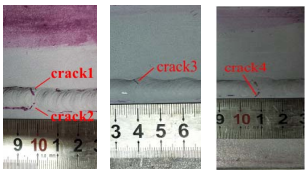

Fig. 23. The penetration results of weld cracks.

(a) (b)

Fig. 24. The amplified result of crack1(60×). (a) The original picture. (b) The amplified result.

the sample. The crack model of the four different cracks on two samples are shown in Fig.22. The penetration testing (PT) results of the four cracks are shown in Fig.23. As the defect size by using PT is the amplification of the real defect size, the real defect is difficult to be found by eyes. Fig.24 is the 60 times amplified results of the crack 1 as shown in Fig.23. It can be seen that the crack is discontinuous. Thus, the conductivity of the crack is not absolutely 0, which increases the detection difficulty. In addition, the thermal pattern maybe different from that of the artificial crack. The validate experiments on the welding cracks include two circumstance: various vertical and horizontal lift-off distance between sensing and defect.

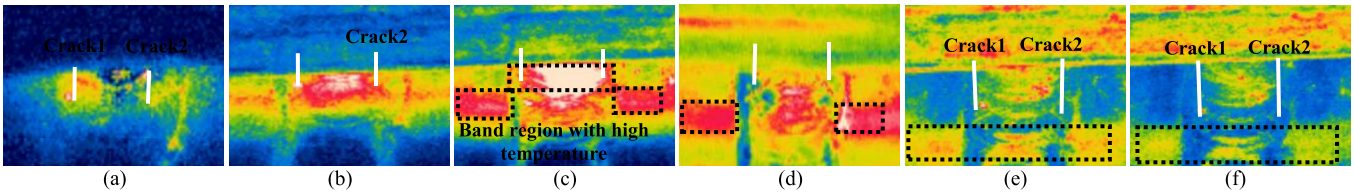

Fig. 25. The experiment results with different lift-off distance (crack 1 and crack 2). (a) h = 2mm. (b) h = 4mm. (c) h = 6mm. (d) h = 7mm. (e) h = 8mm. (f) h = 10mm.

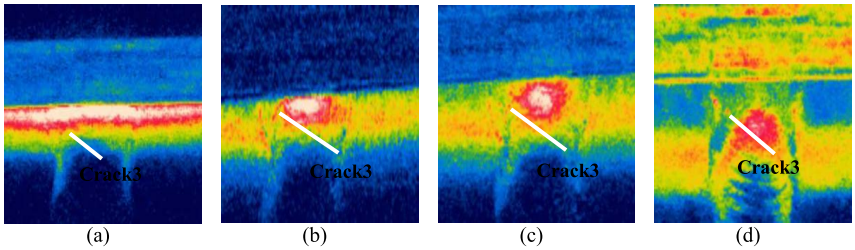

Fig. 26. The experiment results with different lift-off distance (crack 3). (a) h = 2mm. (b) h = 4mm. (c) h = 6mm. (d) h = 9mm.

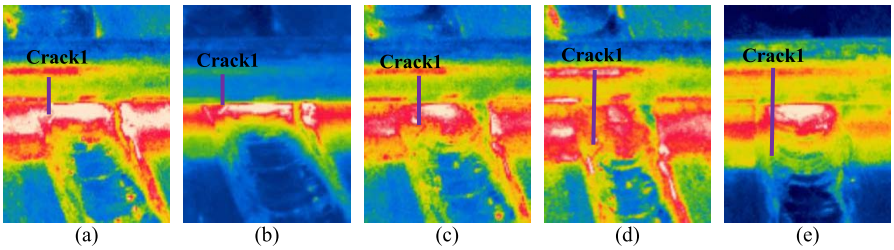

Fig. 27. The experiment results of different horizontal distance between sensing and crack (crack 1). (a) m = 2.5mm. (b) m = 3.5mm. (c) m = 4.5mm. (d) m = 5.5mm. (e) m = 6.5mm.

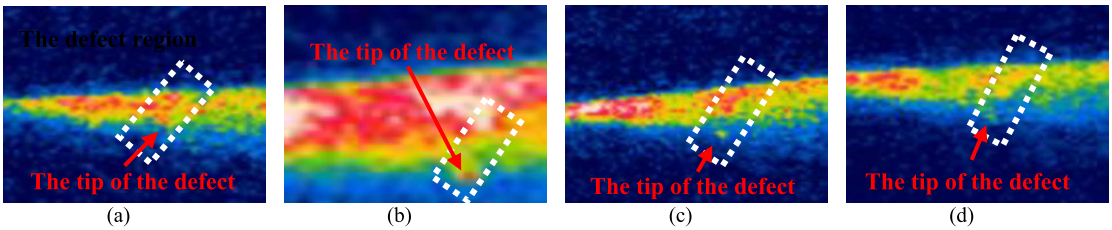

Fig. 28. The experiment results of different horizontal distance between sensing and effect (crack 4). (a) m = 3.5mm. (b) m = 4.5mm. (c) m = 5.5mm. (d) m = 6.5mm.

1) Verification Experiment Under Different Vertical Lift-Off Distance: The experiment results of crack 1 and crack 2 under the different vertical lift-off distance are shown in Fig.25. The various lift-off distance used for testing are 2mm, 4mm, 6mm, 7mm, 8mm and 10mm, respectively. As the cracks are discontinuous (Fig.24 (b)), the thermal pattern is different with artificial cracks which conclude two hot pots on the tip of the crack. The results in Fig.25 (a) indicate that when the lift-off distance is too small, the crack signal is weak and it is submerged by the strong noise. In Fig.25 (b) and (c), part of crack 1 and crack 2 can be seen as they are submerged by the hot temperature regions on the weld. In Fig.25 (d), the crack signal is strong and can be extracted from the noise. In Fig.25 (e) and (f), both noise and signal of crack are weak. Thus, the optimal detecting lift-off distance is 7mm.

From Fig.25, it can be noticed that the coil generates a band region with high temperature (Fig.25(c)). The weld reinforce is 2mm, which means the vertical lift-off distance between the coil and the base material is bigger than that between the coil and the welding material. Thus, the band region on the welding material and the band region on the base material is not in a line. Similarly, when the crack is located within the region, it will be submerged by the strong noise. In Fig.25 (d), since the crack 1 and crack 2 are separated from the band region, they can be successfully detected.

Fig.26 shows the detection results of the crack 3 under the different vertical lift-off distance. In Fig.26 (a), part of crack 3 is submerged by the band region. In Fig.26 (d), a hot pot can be seen in the crack position while it is suffered from a strong noise. Fig.26 (b) and (c) shows the crack clearly, of which

TABLE II
SIMULATION AND EXPERIMENT RESULTS OF OPTIMAL DISTANCE

	Defect	Vertical lift-off distance(mm)	Horizontal distance between sensing and defect(mm)	The optimal distance	
				Vertical	Horizontal
Simulation	$l \times w \times d$:1mm×0.2mm×0.3mm	1, 2, 3, 4, 5, 10, 20	Fixed at 1	3	
	$l \times w \times d$:1mm×0.2mm×0.3mm	Fixed at 5	2, 3, 3.5, 4, 4.5, 5, 6		4
Experiment	Crack 1 and crack 2	2, 4, 6, 7, 8, 10	Fixed at 0	7	
	Crack 3	2, 4, 6, 9	Fixed at 0	4	
	Crack 1	Fixed at 2	2.5, 3.5, 4.5, 5.5, 6.5		5.5
	Crack 4	Fixed at 2	3.5, 4.5, 5.5, 6.5		5.5

TABLE III
THE RESULTS OF DIFFERENT SIGNAL PROCESSING METHOD

h	Original	PCA	ICA	TSR	PPT
2mm	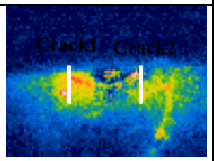	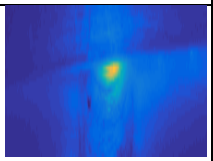	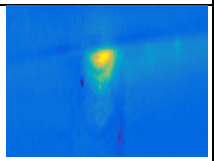	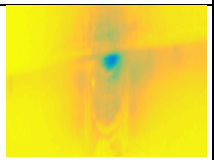	
4mm	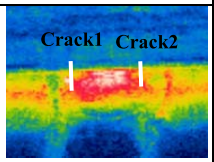	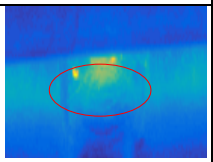	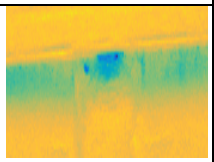	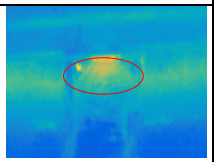	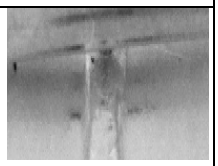
6mm	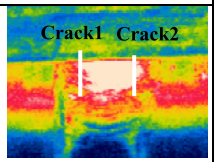	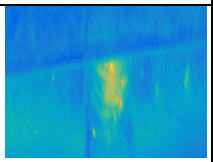	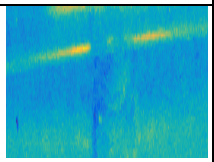	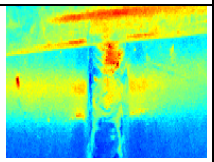	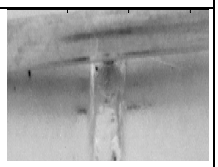
7mm	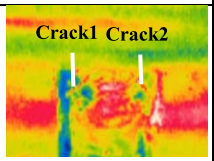	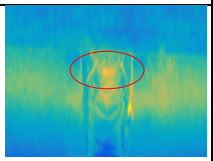	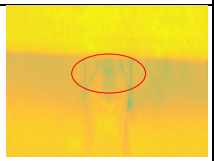	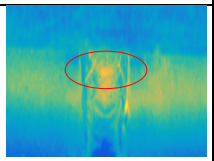	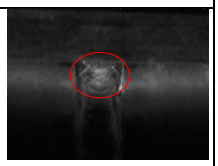
8mm	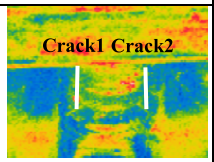	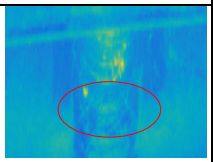	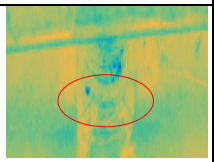	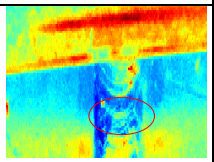	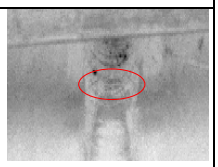
10mm	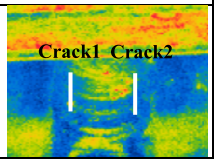	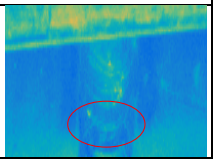	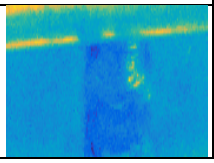	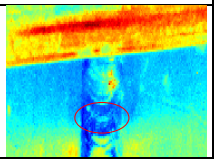	

the former is better. The optimal detecting lift-off distance for crack 3 is 4mm.

2) Verification Experiment Under Different Horizontal Distance Between Sensing and Defect: To verify the effect of the horizontal sensing region on the detection, experiments under different horizontal distance between sensing and defect were carried out. Fig.27 shows the detection results for crack 1 in Fig.23, It can be seen that the crack is submerged by the noise caused by the coil in Fig.27 (a) and (b), and it is separated from the strong noise in Fig.27 (c) and (d) while this eventually cannot be seen in Fig.27 (e).

Fig.28 shows the detection result for crack 4. In the detection results, the tip near the coil is submerged by the noise caused by the coil, the tip which far from the coil can be seen in Fig.28(c). When the horizontal distance between sensing and defect is too small, the crack is totally submerged

(Fig.28 (a)) or cannot be separated from the noise (Fig.28 (b)). When the distance is too far, the crack signal is too weak (Fig.28 (d)).

Results have shown that the best horizontal distance between sensing and defect for crack 1 is 5.5mm, and for crack 4 it is 5.5mm.

The verification experiments for region sensing under different vertical and horizontal lift-off distance between sensing and defect are consistent with the simulations. It is noticed that the distance is related to the permeability of the material, the excitation current and the crack size. The permeability of the material and the excitation current affects the eddy current distribution (Eqn.4 and 5). The crack size affects the disturbance of eddy current around the crack, thus has influence on the require of uniformity. Table II shows the optimal sensing distance (vertical and horizontal lift-off distance between sensing and the defect) under different experiment conditions. 'Fixed at 0' means that the cracks are beneath the coil.

3) Validation Study of the Proposed Region Electromagnetic Sensing Thermography Beyond the Common Thermography Algorithms: The study on the region sensing thermography provides a possibility to dramatically increasing the thermal contrast between the defect and non-defect areas for weak thermal signal detection.

By taking the experiment results with different lift-off distance (crack 1 and crack 2, shown in Fig.18), several common post-processing methods have been used [42]–[44]. These are Principle Component Analysis (PCA), Independent Component Analysis (ICA), Thermal Signal Reconstruction (TSR) and Pulsed Phase Thermography (PPT). The original results and the processing results are shown in table III.

The results indicate that for $h = 2$mm and 6mm, the post-processing methods cannot detect the cracks effectively, for $h = 4$, 8, and 10mm, part of the methods can detect the cracks with low thermal contrast. Only for the optimized region $h = 7$mm, the methods have a good performance. This confirms that without obtaining the optimal region electromagnetic thermal field, it is difficult to detect the cracks correctly.

IV. Conclusion and Future Work

In this paper, the sensing effect of the region electromagnetic performance is studied. The intensity and uniformity of eddy current under different vertical and horizontal lift-off distance between sensing and defect are investigated. Several conclusions can be drawn:

i). Both the intensity and uniformity of the electromagnetic as well as thermal fields have highly impacts on the crack detection. If the intensity is too low or the uniformity is not sufficient, the crack cannot be detected clearly.

ii). With the increasing of the vertical or the horizontal lift-off distance between sensing and defect, the intensity of the eddy current on non-defective sample decreases and the uniformity increases. There exists a region which has relatively high intensity and uniformity for the electromagnetic and thermal fields. This sensing region will be benefit in detecting cracks with high thermal contrast.

iii). The optimal region sensing for the detection is related to the exciting current, the magnetic permeability of the material, and the crack size.

Future work will study the minimum intensity and uniformity required for weak thermal signal detection. It is required to design a proper sensing structure to obtain uniform electromagnetic and thermal region.

References

[1] W. Yang, P. J. Tavner, C. J. Crabtree, and M. Wilkinson, "Cost-effective condition monitoring for wind turbines," *IEEE Trans. Ind. Electron.*, vol. 57, no. 1, pp. 263–271, Jan. 2010.

[2] N. Kasai, A. Takada, K. Fukuoka, H. Aiyama, and M. Hashimoto, "Quantitative investigation of a standard test shim for magnetic particle testing," *NDT E Int.*, vol. 44, no. 5, pp. 421–426, Sep. 2011.

[3] K. Fukuoka, S. Noma, M. Kobayashi, T. Ozaki, and Y. Oikawa, "Consideration of multi-coil type magnetizer for detection of omnidirectional crack in magnetic particle testing," *Int. J. Appl. Electromagn. Mech.*, vol. 52, nos. 3–4, pp. 1537–1543, 2016.

[4] B. Liu, Y. Zhang, and G. Zhou, "Magnetic particle testing for fillet welds of vertical cylindrical steel storage tank," Tech. Monit. Center Changqing Oilfield Co., CNPC Tubular Goods Res. Istitute, Tech. Rep., 2015.

[5] R. Clark, W. D. Dover, and L. J. Bond, "The effect of crack closure on the reliability of NDT predictions of crack size," *NDT Int.*, vol. 20, no. 5, pp. 269–275, Oct. 1987.

[6] J. Zhao, B. Gao, W. L. Woo, F. Qiu, and G. Y. Tian, "Crack evaluation based on novel circle-ferrite induction thermography," *IEEE Sensors J.*, vol. 17, no. 17, pp. 5637–5645, Sep. 2017.

[7] F. Syassen, "Method for the detection of a possible joint defect in a friction stir weld seam," U.S. Patent 9182299 B2, Nov. 10, 2015.

[8] S. Ohya, Y. Akimoto, Y. Ohmura, and Y. Hagiwara, "OS4(P)-9(OS04W0127) the detection of internal fatigue crack using X-ray stress measurement," *J. Soc. Mater. Sci. Jpn.*, vol. 51, no. 12, pp. 1423–1428, 2017.

[9] M. Naeimi *et al.*, "Reconstruction of the rolling contact fatigue cracks in rails using X-ray computed tomography," *NDT&E Int.*, vol. 92, pp. 199–212, Dec. 2017.

[10] N. M. Bhattad and S. S. Patil, "System and method for identifying defects in welds by processing X-ray images," *J. Brazilian Soc. Mech. Sci. Eng.*, pp. 1–8, 2015.

[11] S. M. Shepard, J. R. Lhota, B. A. Rubadeux, D. Wang, and T. Ahmed, "Reconstruction and enhancement of active thermographic image sequences," *Opt. Eng.*, vol. 42, no. 5, pp. 1337–1342, 2003.

[12] A. Yin, B. Gao, G. Y. Tian, W. L. Woo, and K. Li, "Physical interpretation and separation of eddy current pulsed thermography," *J. Appl. Phys.*, vol. 113, no. 6, pp. 1907–1921, 2013.

[13] Y. Wang, B. Gao, G. Tian, W. L. Woo, and Y. Miao, "Diffusion and separation mechanism of transient electromagnetic and thermal fields," *Int. J. Thermal Sci.*, vol. 102, pp. 308–318, Apr. 2016.

[14] H. Walaszek, "Comparison between induction thermography and conventional NDT methods for forged parts," *Current Orthopaedics*, vol. 10, no. 3, p. 205, 1996.

[15] M. Morozov, G. Y. Tian, and P. J. Withers, "Noncontact evaluation of the dependency of electrical conductivity on stress for various Al alloys as a function of plastic deformation and annealing," *J. Appl. Phys.*, vol. 108, no. 2, p. 024909, 2010.

[16] J. Wilson, G. Tian, I. Mukriz, and D. Almond, "PEC thermography for imaging multiple cracks from rolling contact fatigue," *NDT&E Int.*, vol. 44, no. 6, pp. 505–512, 2011.

[17] Y. Gao *et al.*, "Electromagnetic pulsed thermography for natural cracks inspection," *Sci. Rep.*, vol. 7, Feb. 2017, Art. no. 42073.

[18] R. Yang, Y. He, B. Gao, G. Y. Tian, and J. Peng, "Lateral heat conduction based eddy current thermography for detection of parallel cracks and rail tread oblique cracks," *Measurement*, vol. 66, pp. 54–61, Apr. 2015.

[19] Y. He, G. Y. Tian, M. Pan, D. Chen, and H. Zhang, "An investigation into eddy current pulsed thermography for detection of corrosion blister," *Corrosion Sci.*, vol. 78, pp. 1–6, Jan. 2014.

[20] Z. Liu, G. Lu, X. Liu, X. Jiang, and G. Lodewijks, "Image processing algorithms for crack detection in welded structures via pulsed eddy current thermal imaging," *IEEE Instrum. Meas. Mag.*, vol. 20, no. 4, pp. 34–44, Aug. 2017.

[21] P. Rettenmeier, E. Roos, and S. Weihe, "Fatigue analysis of multiaxially loaded crane runway structures including welding residual stress effects," *Int. J. Fatigue*, vol. 82, pp. 179–187, Jan. 2016.
[22] B. Gao, Y. He, W. L. Woo, G. Y. Tian, J. Liu, and Y. Hu, "Multidimensional tensor-based inductive thermography with multiple physical fields for offshore wind turbine gear inspection," *IEEE Trans. Ind. Electron.*, vol. 63, no. 10, pp. 6305–6315, Oct. 2016.
[23] J. Peng, G. Y. Tian, L. Wang, Y. Zhang, K. Li, and X. Gao, "Investigation into eddy current pulsed thermography for rolling contact fatigue detection and characterization," *NDT&E Int.*, vol. 74, pp. 72–80, Sep. 2015.
[24] Y. He, G. Tian, M. Pan, and D. Chen, "Eddy current pulsed phase thermography and feature extraction," *Appl. Phys. Lett.*, vol. 103, no. 8, p. 084104, 2013.
[25] N. Biju, N. Ganesan, C. V. Krishnamurthy, and K. Balasubramaniam, "Frequency optimization for eddy current thermography," *NDT&E Int.*, vol. 42, no. 5, pp. 415–420, Jul. 2009.
[26] B. B. Lahiri *et al.*, "Infrared thermography based defect detection in ferromagnetic specimens using a low frequency alternating magnetic field," *Infr. Phys. Technol.*, vol. 64, pp. 125–133, May 2014.
[27] H. Shen, Z. Q. Yao, Y. J. Shi, and J. Hu, "Study on temperature field induced in high frequency induction heating," *Acta Metallurgica Sinica (English Lett.)*, vol. 19, no. 3, pp. 190–196, 2006.
[28] B. Oswald-Tranta, "Thermo-inductive crack detection," *Nondestruct. Test. Eval.*, vol. 22, nos. 2–3, pp. 137–153, 2007.
[29] K. Li, G. Y. Tian, L. Cheng, A. Yin, W. Cao, and S. Crichton, "State detection of bond wires in IGBT modules using eddy current pulsed thermography," *IEEE Trans. Power Electron.*, vol. 29, no. 9, pp. 5000–5009, Sep. 2014.
[30] N. Tsopelas and N. J. Siakavellas, "Performance of circular and square coils in electromagnetic–thermal non-destructive inspection," *NDT&E Int.*, vol. 40, no. 1, pp. 12–28, 2007.
[31] Y. Gao, G. Y. Tian, P. Wang, H. Wang, J. Ji, and S. Ding, "Ferrite-yoke based pulsed induction thermography for cracks quantitative evaluation," in *Proc. IEEE Far East NDT New Technol. Appl. Forum.*, May 2015, pp. 197–201.
[32] Y. Gao, G. Y. Tian, K. Li, J. Ji, P. Wang, and H. Wang, "Multiple cracks detection and visualization using magnetic flux leakage and eddy current pulsed thermography," *Sens. Actuators A, Phys.*, vol. 234, no. 6, pp. 269–281, Oct. 2015.
[33] K. A. Hansen and E. C. Weisberg, "Asymmetric induction work coil for thermoplastic welding," U.S. Patent 5 444 220 A, Aug. 22, 1995.
[34] U. Netzelmann, G. Walle, S. Lugin, A. Ehlen, S. Bessert, and B. Valeske, "Induction thermography: Principle, applications and first steps towards standardisation," *Quant. Infr. Thermography J.*, vol. 13, no. 2, pp. 170–181, 2015.
[35] J. Vrana, M. Goldammer, J. Baumann, M. Rothenfusser, and W. Arnold, "Mechanisms and models for crack detection with induction thermography," *AIP Conf. Proc.*, vol. 975, no. 1, pp. 475–482, 2008.
[36] H. C. Choe, T. J. Meitzler, and G. R. Gerhart, "Background and target randomization and root mean square (RMS) background matching using a new deltaT metric definition," *Proc. SPIE*, vol. 1967, pp. 560–573, Aug. 1993.
[37] J. A. D'Agostino, W. Lawson, and L. Wilson, "Concepts for search and detection model improvements," *Proc SPIE*, vol. 3063, pp. 14–22, Jun. 1997.
[38] B. Gao, Y. He, W. L. Woo, G. Y. Tian, J. Liu, and Y. Hu, "Multidimensional tensor-based inductive thermography with multiple physical fields for offshore wind turbine gear inspection," *IEEE Trans. Ind. Electron.*, vol. 63, no. 10, pp. 6305–6315, 2016.
[39] E. M. Abdul-Baki, A. H. Ahmad, F. A. Abood, and A. F. Batti, "Modeling of induction heating process of a conducting ferromagnetic materials," *J. Eng.*, vol. 15, no. 4, pp. 4321–4338, 2009.
[40] F. Leach and I. Vadan, "FEM modeling of a continuous induction heating process of steel wire hardening," *Steel Wire*, 2010.
[41] Y. Wang, G. Tian, and B. Gao, "Eddy current and thermal propagation for quantitative NDT&E," in *Proc. 19th World Conf. Non-Destructive Test.*, 2016, pp. 1–9.
[42] C. Xu, X. Gong, W. Zhang, and G. Chen, "An investigation on eddy current pulsed thermography to detect surface cracks on the tungsten carbide matrix of polycrystalline diamond compact bit," *Appl. Sci.*, vol. 7, no. 4, p. 429, 2017.
[43] C. Xu, J. Xie, G. Chen, and W. Huang, "An infrared thermal image processing framework based on superpixel algorithm to detect cracks on metal surface," *Infr. Phys. Technol.*, vol. 67, no. 4, pp. 266–272, Nov. 2014.
[44] A. Yin, Y. Gou, H. Ran, and J. Li, "Thermography multidimensional manifold space projection and principal curves extraction for material state evaluation," *Jpn. J. Appl. Phys.*, vol. 56, no. 8, p. 086601, 2017.

Yingchun Wu received the B.Sc. degree from the College of Electrical Engineering, Zhengzhou University, Zhengzhou, China, in 2016. She is currently pursuing the M.Sc. degree in nondestructive testing using induction thermography technique with the University of Electronic Science and Technology of China, Chengdu, China. Her research interests include region electromagnetic sensing thermography and the speed effect based on rail nondestructive testing.

Bin Gao (M'12–SM'14) received the B.Sc. degree in communications and signal processing from Southwest Jiao Tong University, China, in 2005, and the M.Sc. degree (With Distinction) in communications and signal processing and the Ph.D. degree from Newcastle University, U.K., in 2011. From 2011 to 2013, he was a Research Associate with Newcastle University, working on wearable acoustic sensor technology. He is currently a Professor with the School of Automation Engineering, University of Electronic Science and Technology of China, Chengdu, China. His research interests include sensor signal processing, machine learning, social signal processing, nondestructive testing and evaluation, where he actively publishes in these areas. He is also a very active reviewer for many international journals and long standing conferences. He has coordinated several research projects with the National Natural Science Foundation of China.

Jian Zhao received the B.Sc. degree in electrical engineering and automation from Chengdu University of Technology, Chengdu, China, in 2015. He is currently pursuing the M.Sc. degree in nondestructive testing using induction thermography technique with the University of Electronic Science and Technology of China, Chengdu. His research interests include induction thermography, Internet of Things technology, and data mining.

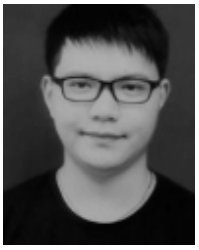

Yizhe Wang received the B.Sc. degree in physics from Shenyang Normal University, Shenyang, China, in 2012, and the M.E. degree in instrument science and technology from the University of Electronic Science and Technology of China (UESTC), Chengdu, China, in 2014. He is currently pursuing the Ph.D. degree in quantitative fatigue assessment and health state monitoring using infrared thermography with UESTC and Laval University, Quebec, QC, Canada. His current research interests include sensor design, fatigue damage, quantitative nondestructive testing and evaluation, sensor signal processing, and machine learning.

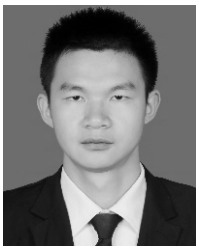

Zewei Liu received the B.Sc. degree in automation from Henan Polytechnic University, Jiaozuo, China, in 2017. He is currently pursuing the M.Sc. degree in nondestructive testing using induction thermography technique with the University of Electronic Science and Technology of China, Chengdu, China. His research interests include automated eddy current thermography and optimization.

Juan Chen received the B.S. degree in power engineering and engineering thermophysics from the China University of Petroleum (East China), China, in 2005, and the M.Sc. degree in power engineering and engineering thermophysics from Chongqing University, China, in 2011. She is currently an Engineer with the Sichuan Special Equipment Inspection Institute, China. Her work and research interests include equipment inspection.

Ying Yin received the B.Eng. degree in electrical engineering from Xihua University in 2005 and the Ph.D. degree in digital image processing from Newcastle University in 2009. He is currently a Senior Engineer and the Director of the Research Department of Sichuan Special Equipment Inspection Institute. His major research includes non-destructive testing and evaluation for special equipment specifically, image processing.

Gui Yun Tian (M'01–SM'03) received the B.Sc. degree in metrology and instrumentation and the M.Sc. degree in precision engineering from the University of Sichuan, Chengdu, China, in 1985 and 1988, respectively, and the Ph.D. degree from the University of Derby, Derby, U.K., in 1998. From 2000 to 2006, he was a Lecturer, a Senior Lecturer, a Reader, a Professor, and the Head of the Group of Systems Engineering, respectively, with the University of Huddersfield, U.K. Since 2007, he has been with Newcastle University, Newcastle upon Tyne, U.K., where he has been the Chair Professor in Sensor Technologies. He is currently an Adjunct Professor with the School of Automation Engineering, University of Electronic Science and Technology of China. He has coordinated several research projects from the Engineering and Physical Sciences Research Council, Royal Academy of Engineering and FP7, on top of this he also has good collaboration with leading industrial companies, such as Airbus, Rolls Royce, BP, nPower, Networkrail, and TWI.